IDENTIFICATION OF STIFFNESS AND DAMPING COEFFICIENTS IN A SHOED BRUSH SEAL

Adolfo Delgado
Research Assistant
adelgam@neo.tamu.edu

Luis San Andrés
Professor
lsanandres@mengr.tamu.edu

Turbomachinery Laboratory
Texas A&M University
College Station, TX 77843-3123, USA

John F. Justak
Advance Turbomachinery Solutions
P.O. BOX 442, Stuart, FL 34995, USA
JUSTAK_research@attglobal.net

RESUMEN

El sello de brocha metálica con múltiple zapatas es una variación del sello de brocha convencional. Zapatas de metal arqueadas son soldadas a la terminación de las cerdas en el sello. Este diseño permite rotación de flecha en ambos sentidos y disminuye el desgaste del sello ya que las zapatas, originalmente en contacto con el rotor, se despegan de éste debido a la generación de la película hidrodinámica durante rotación. Los coeficientes de rigidez estructural del sello son determinados a partir de ensayos de compresión aplicados a un sello de brocha de 11 pulgadas de diámetro (36 zapatas). Los coeficientes de rigidez y amortiguamiento dinámico son derivados de funciones de transferencia obtenidas a partir de pruebas de impacto externo aplicados al sello. Los ensayos de compresión incluyen dos modalidades, con y sin perturbación. La perturbación consiste en impactar el sello levemente hasta que éste alcance una posición de equilibrio. Estas dos modalidades permiten constatar los efectos de la fricción seca presentes en la interacción de las cerdas entre si, y la interacción entre éstas y la superficie del anillo posterior donde se asienta el sello. Los resultados de los ensayos de impacto muestran comportamientos no lineales asociados a los efectos de la fricción seca. Los coeficientes de rigidez del sello son también obtenidos analíticamente modelando cada cerda como una viga simple sometida a flexión.

ABSTRACT

The multiple-shoe brush seal, a variation of a standard brush seal, comprises of multiple arcuate thin metal shoes spot-welded to the brush seal bristle bead. This novel brush seal type allows for reverse shaft rotation with reduced wear since, during rotor spinning, the shoes lift off due to hydrodynamic effects. Static load pull tests on a 36-shoe brush seal, 11 inches in diameter, and recorded seal radial displacements enable the identification of the seal structural stiffness coefficients. Dynamic seal stiffness and effective viscous damping coefficients are derived from transfer functions obtained from impact loads exerted on the test element. While conducting the static load tests, conditions of perturbing (tapping) or not perturbing the seal element evidence dry friction (stick-slip) effects arising from bristle to bristle and bristle bed to back plate interactions. Seal stiffnesses are larger for the non-tapping condition. The impact test results show typical nonlinearities associated to dry friction effects. An ensemble-shoes model that considers the bristles as simple beams under flexure renders a simple formula for prediction of the stiffness coefficient of the whole shoed-brush seal. Predictions validate the identified seal static stiffness.

NOMENCLATURE

a_s	Shoed brush seal acceleration (m/s^2)
A	Bristle area (in^2)
C_s	Shoed brush seal Damping coefficient (N-s/m)
d_b	Distance from pad center to bristle tip (in)
E	Bristle modulus of elasticity (psi)
f_{z1}, f_{z2}	Bristle end reaction forces (lbf)
fx, fy	Bristle end reaction forces (lbf)
f_{sXX},f_{sYY}	Shoed brush seal flexibility coefficients (in/lbf)
f_{sXY},f_{sYX}	Shoed brush seal cross-coupled flexibility coefficients (in/lbf)
F	Shoed brush-seal reaction force (lbf)
F_s	Impact force amplitude (lbf)
I	Bristle area moment of inertia (in^4)
K	Shoed brush seal stiffness matrix consistent with constraints (lbf/in)
$K_{s=}$ K_{sXX}, K_{sYY}	Shoed brush seal stiffness coefficients (lbf/in)
$k_{s=}$ K_{sXY}, K_{sYX}	Shoed brush seal cross-coupled stiffness coefficients (lbf/in)
$K_{i,j\ \ i,j=x,y,\varphi}$	Single pad stiffness coefficients (lbf/in)
K_{pe}	Single pad stiffness matrix consistent with constraints (lbf/in)
k_p	Single pad stiffness for radial load (lbf/in)
L	Bristle length (in)
L_p	Pad arcuate length (in)

m_z	Bristle reaction moment (lbf-in)
M_s	Shoed brush seal mass (Kg)
n	Bristle number, starting from pad leading edge
N_b	Number of bristles in one row per pad length
N_r	Number of rows of bristles per pad
N_{pad}	Number of pads on seal
T	Orthogonal coordinate transformation matrix
(X,Y)	Inertial coordinate system attached to rotor center
$X_i:(x_i, y_i, C_i)$ $i=bf,bw$	Coordinates for bristle end motion (x parallel to pad arcuate length)
$X_p:(x_p, y_p, \varphi_p)$	Coordinates for pad motion (x parallel to pad arcuate length)
(z_1, z_2, φ_b)	Coordinates for bristle end motion (z_1 parallel to bristle axis)
θ	Bristle lay angle (deg)
Θ_p	Circumferential location of pad.
φ	Pad rotation, bristle end rotation
ω	Vibration frequency (rad/s)

SUBINDEXES

b	Bristle
bf	Free-end bristle
bw	Spot welded bristle
p	Pad
pe	Pad equivalent
s	Seal

INTRODUCTION

Leakage (secondary) flows between stages influence the overall efficiency of a gas turbine. Improvements to reduce leakage can lead to an increase in thrust, as much as 17 %, and a decrease over 7 % in specific fuel consumption [1]. For over 60 years, labyrinth seals have been the primary seal used in gas turbines [2]. However, leakage through these seals increases with operation due to wear induced by thermal growth and rotor excursion. In past years, these disadvantages have become a major concern because of increased turbine inlet temperatures, desired larger efficiencies and more severe operating conditions in modern aircraft engines.

Brush seals have emerged as a novel sealing technology that can effectively reduce interstage leakage in gas turbines. Brush seals also have the ability to handle larger vibrations (over 0.025in. amplitude [3]) and require less axial space when compared to labyrinth seals, for example. Current research demonstrates that replacing the best knife-edge labyrinth seal with a brush seal leads to a 90 % reduction in internal leakage on secondary air flow systems [4]. Also, based on initial tests, brush seals have shown favorable rotordynamic characteristics as compared to labyrinth configurations, for example, thus assuring rotordynamic stability [5].

The brush seal is an annular contact seal rather than a cavity annular seal (labyrinth seal), thus producing sustained wear and local thermal distortion. Bristle material and rotor coating are important in manufacturing reliable brush seals. Besides wear, conventional brush seals cannot function in a reverse shaft rotation mode, preventing their use in certain aircraft engines where counter rotations are needed to control wing maneuvers. Recall that a brush seal consists of a set of densely packed metal bristles placed on the inner side of a cylindrical structure. The bristles are angled in the direction of shaft rotation. This particular arrangement allows the bristles to bend rather than buckle during shaft orbital motions. Operation in a reverse rotation mode destroys the seal.

Justak [6] introduced a novel brush seal design that incorporates metal shoes at the free end of the bristles to allow rotor motion in both directions (see Figure 1). This particular variation reduces wear since the shoes should lift off due to hydrodynamic effects during rotor spinning [6]. This novel design is still in the development stages and requires extensive testing. The main concerns are to maintain the leakage performance of standard brush seals while decreasing wear and allowing reverse rotation.

An analysis for prediction of the structural stiffness of a shoed brush seal follows. The analysis is based on the ensemble of single bristle stiffnesses attached to a pad. Measurements of the brush seal deflection due to applied loads allow the identification of the seal stiffness and validate the model predictions.

ANALYSIS

Stiffness of a single bristle

Each bristle in the pad assembly is cantilevered to the brush seal base with the opposite end interacting with the pad. Figure 2 shows a schematic of a single pad and a bristle. From elastic beam theory, the reactions and moment of the bristle due to displacements and rotations of its end are

$$\overline{F_b} = \begin{Bmatrix} f_{z1} \\ f_{z2} \\ m_z \end{Bmatrix} = -\begin{bmatrix} A\cdot E/L & 0 & 0 \\ 0 & 12E\cdot I/L^3 & -6E\cdot I/L^2 \\ 0 & -6E\cdot I/L^2 & 4E\cdot I/L \end{bmatrix} \cdot \begin{Bmatrix} z_1 \\ z_2 \\ \phi_b \end{Bmatrix} = -\overline{K_b} \cdot \begin{Bmatrix} z_1 \\ z_2 \\ \phi_b \end{Bmatrix} \quad (1)$$

Within a pad, there are two types of bristle to pad interactions: pinned (free end) and spot welded (fixed end). In a pinned bristle not welded to a pad, its free end can rotate unrestrained while the bristle end translational displacements are defined by the pad displacements. Hence, the reaction moment, m_z, of a free bristle is null and the bristle reaction forces reduce to

$$\overline{F_{bf}} = \begin{Bmatrix} f_{z1} \\ f_{z2} \end{Bmatrix} = -\begin{bmatrix} AE/L & 0 \\ 0 & 3EI/L^3 \end{bmatrix} \cdot \begin{Bmatrix} z_1 \\ z_2 \end{Bmatrix} = -\overline{K_{bf}} \cdot \begin{Bmatrix} z_1 \\ z_2 \end{Bmatrix} \quad (2)$$

The bristle reaction forces $(f_{z1}, f_{z2})^T$ can be expressed as $(fx_{bf}, fy_{bf})^T$ using an orthogonal transformation, i.e.

$$F_{bf} = \begin{Bmatrix} fx_{bf} \\ fy_{bf} \end{Bmatrix} = -T_{bf}^{\mathrm{T}} \cdot \overline{K_{bf}} \cdot T_{bf} \cdot X_{bf} = -K_{bf} \cdot X_{bf} \qquad (3)$$

The bristle end displacements vector is represented in terms of the pad displacement vector using the following relation

$$X_{bf} = \begin{bmatrix} 1 & 0 & 0 \\ 0 & 1 & d_b \end{bmatrix} \cdot \begin{Bmatrix} x_p \\ y_p \\ \phi_p \end{Bmatrix} = T_{pbf} \cdot X_p \qquad (4)$$

where

$$d_b = L_p \left(\frac{n-1}{N_b - 1} \right) - \frac{L_p}{2} \qquad (5)$$

The forces exerted on the pad by the bristle are simply the reaction forces due to the bristle displacements, while the moment exerted on the pad is the cross product of the moment arm (d_b) and the normal force (fy_{bf}). Thus, the stiffness matrix of a single bristle due to the pad displacements (x_p, y_p, ϕ_p) becomes

$$K_{pbf} = T_{pbf}^{\mathrm{T}} \cdot K_{bf} \cdot T_{pbf} = T_{pbf}^{\mathrm{T}} \cdot T_{bf}^{\mathrm{T}} \cdot \overline{K_{bf}} \cdot T_{bf} \cdot T_{pbf} \qquad (6)$$

Unlike the free bristle, a bristle tip spot welded to a pad has the same angular displacement as the pad, i.e. $\phi_b = \phi_p$. Therefore, the reaction forces and moment of the bristle tip are

$$\overline{F_{bw}} = \overline{F_b} = -\overline{K_b} \cdot \begin{Bmatrix} z_1 \\ z_2 \\ \phi_b \end{Bmatrix} = -\overline{K_{bw}} \cdot \begin{Bmatrix} z_1 \\ z_2 \\ \phi_b \end{Bmatrix} \qquad (7)$$

Thus, the stiffness matrix of a single bristle due to the pad displacements (x_p, y_p, ϕ_p), following the previous procedure, is

$$K_{pbw} = T_{pbw}^{\mathrm{T}} \cdot K_{bw} \cdot T_{pbw} = T_{pbw}^{\mathrm{T}} \cdot T_{bw}^{\mathrm{T}} \cdot \overline{K_{bw}} \cdot T_{bw} \cdot T_{pbw} \qquad (8)$$

Shoed Brush Seal Static Stiffness

The analysis considers that there is interference fit between the rotor and the shoes of the brush seal, i.e. all pads are in contact with the rotor surface. For simplicity the (static) friction between the pad and rotor surface is neglected, and thus a pad can only support normal loads, perpendicular to the pad arc. That is, the tangential force (fx_p) to the pad must be zero. Given a radial rotor displacement causes the pads to retract (displace) along directions perpendicular to their arcs; and hence, a pad does not rotate[1].

Under this loading condition, i.e. no pad rotation (ϕ_p=0), the requirement that the tangential force (fx_p) equals zero, gives an expression for the normal force

$$f_{yp} = k_p y_p, \qquad k_p = K_{yy} - \frac{K_{xy} K_{yx}}{K_{xx}} \qquad (9)$$

where k_p represents the equivalent stiffness of the pad consistent with the constraints imposed. The total shoed-brush seal stiffness (K_s) follows from the assembly of the stiffness for each pad around the rotor circumference, i.e.

$$K_s = \sum_{p=1}^{N_{pad}} \begin{bmatrix} \cos\Theta_p & \sin\Theta_p \\ -\sin\Theta_p & \cos\Theta_p \end{bmatrix} \cdot K_{pe} \cdot \begin{bmatrix} \cos\Theta_p & -\sin\Theta_p \\ \sin\Theta_p & \cos\Theta_p \end{bmatrix} \qquad (10)$$

where

$$K_{pe} = \begin{bmatrix} 0 & 0 \\ 0 & K_{yy} - \dfrac{K_{xy} K_{yx}}{K_{xx}} \end{bmatrix} \qquad (11)$$

For $N_{pad}>2$, the expression above reduces to:

$$K_s = \begin{bmatrix} \frac{N_{pad}}{2} k_p & 0 \\ 0 & \frac{N_{pad}}{2} k_p \end{bmatrix} = \begin{bmatrix} K_{sXX} & K_{sXY} \\ K_{sYX} & K_{sYY} \end{bmatrix} \qquad (12)$$

The shoed brush seal is an isotropic structure, i.e. $K_{sXX} = K_{sYY}$, since the seal assembly is rotationally symmetric. No cross-coupled stiffnesses appear since no (dry) friction is accounted for in the model. The experimental results validate the model assumptions and predictions.

EXPERIMENTAL FACILITY

Experiments to determine the test brush seal static stiffness were conducted using an ad-hoc test set up. Figure 3 shows the test fixture with the following components:

a) a brush seal mounted on a larger steel ring of 12.5 inches outside diameter and 0.34 inches in length.
b) a fixed disk of 12.1 inches diameter on which the brush seal is mounted. The diametral interference is 0.016 in.
c) Four (90^0 apart) guide posts hold the brush seal into a flat plate. These posts allow a clearance of at most 0.001±0.0005 inches to prevent axial motions of the seal.
d) Two dial indicators, positioned along the vertical and horizontal directions.
e) A bottom hook for application of the static loads on the seal.

Table 1 presents the dimensions and material properties of the seal tested. Impact tests on the seal structure were also conducted using the same set up, and incorporating a miniature piezoelectric accelerometer (1 gram) and a calibrated hammer instead of dial indicators.

[1] Under hydrodynamic operation (rotor spinning) a pad will lift off from the rotor surface and then it can both rotate and displace laterally.

EXPERIMENTAL PROCEDURE

The static experiments consisted of applying known (calibrated) weights on the seal and recording the ring displacements in two orthogonal directions (x and y). Multiple sets of pull forces and ensuing displacements were obtained. Two types of measurement procedures, with tapping and non tapping on the seal ring, reveal the effect of dry friction arising from the bristle-to-bristle interactions. This effect is most important for the correct interpretation of the results obtained from the experiments. Each test consists of two independent measurements along two orthogonal axes, i.e. 90 degrees apart.

At the beginning of each test, the seal ring holder was tapped slightly with a rubber hammer to set the initial equilibrium position. This random process followed until a static position was apparent, i.e. did not change over time or with further tapping. Neither the applied load nor the frequency of tapping could be measured. The tapping process was necessary to overcome the relatively high friction forces preventing the brush seal to reach an actual equilibrium position. Tapping generates motion that breaks the contact forces between the bristles and allows sliding motion among them.

The static loading process began once the gauges (horizontal and vertical) were zeroed after the initial tapping process. The methodology followed in the loading process for the tapping tests consists of three steps: applying statically a weight to the seal ring, recording displacements, removing the (whole) weight, and tapping the seal to overcome dry friction forces. In the non-tapping tests, no perturbation was introduced after the loading step. Between 8 to 10 loading cycles were conducted, depending on the type of test, ranging from 1 to 9 pounds.

Experiments proceeded to measure the transient response of the seal ring when excited by impact loads exerted by a calibrated hammer. The experiments aim to identify the natural frequency of the brush seal and ring assembly, to elucidate the nature of damping arising from the brush seal, and to estimate the seal structure dynamic stiffness and (viscous equivalent) damping coefficients. Each test consisted of 20 impacts that are averaged and processed by a frequency analyzer. The frequency span of the seal dynamic response ranged from 20 Hz to 500 Hz.

EXPERIMENTAL RESULTS

Figures 4 and 5 depict the brush seal deflections, along the principal and cross-directions, versus the statically applied loads. The cross-direction is 90 degrees away from the load direction. The results shown correspond to an average for the three seal orthogonal positions with tapping, and for two orthogonal orientations for non-tapping. Each symbol represents an average deflection representative of the configurations tested.

The seal stiffness coefficients are obtained from the recorded flexibilities (f_s) as,

$$K_s = \frac{f_{sXX}}{f_{sXX}^{\,2} - f_{sXY}^{\,2}} = K_{sXX} = K_{sYY} \tag{13}$$

$$k_s = \frac{-f_{sXY}}{f_{sXX}^{\,2} - f_{sXY}^{\,2}} = K_{sXY} = -K_{sYX} \tag{14}$$

Table 2 details the mean values of seal flexibilities and stiffness coefficients obtained from the static load and seal deflection measurements. The cross-deflections, i.e. orthogonal to the applied force, are at least one order of magnitude smaller than the deflections in the (principal) direction along the applied load. The brush seal (average) direct stiffness (K_s) resulting from the tests with tapping and not tapping is 231.6 lb/in and 331.2 lb/in, respectively.

For the test seal, the bristle density ($d_b\ N_b/L_p$) equals 0.903, denoting a very compact bristle bed. The two thin spot welds are located at approximately 24% and 71% of the pad length. The predicted seal stiffness coefficients ($K_{sXX} = K_{sYY}$) are 225.24 lbf/in. The predicted value (tapping) lies well within the measurement uncertainty of 18.5 lbf/in (see Table 2). Recall that tapping the seal diminishes the effects of the friction force on the seal, making the results suitable for comparison with the current theoretical model.

Figure 6 displays a typical impact load and the ensuing seal acceleration transient response. The bottom graphs show the average frequency response of the applied load and seal response due to twenty consecutive impacts. The FFT of the seal acceleration (and time response as well) show decaying motions at a natural frequency of 408 Hz. The time decay responses show peak amplitudes decreasing linearly with time, characteristic of a mechanical system with dry friction.

Figure 7 shows the (frequency averaged) transfer function of acceleration over applied load and the coherence function resulting from the 20 impacts. The coherence function is close to one over large spans of frequency, including the natural frequencies, thus giving confidence in the test results. The acceleration FFT also shows a region of small peak amplitudes within a broad frequency band from 40 to 80 Hz. Motion within this frequency range is probably related to a first natural frequency (36.5 Hz), although overdamped due to the large dry-frictional effects. This lowest natural frequency is derived from the total mass of the seal with the ring holder (1.7 lb, 0.77 kg) and the stiffness obtained from the tapping tests, i.e. K=231.6 lb/in (40.5 KN/m). The stiffness from tapping tests represents the commanding stiffness, since the impact load is large enough to cause large initial seal displacements that "break" most of the stick-slip contacts within the brush seal bristles as in the case of the static tests including tapping.

The system parameters, stiffness, equivalent viscous damping and mass, (K_s, C_s, M_s), respectively, are derived from a nonlinear curve fit to the amplitude of the test transfer function. For a linear system, the relationship between acceleration (a_s) and force (F_s) is given in the frequency domain as

$$\frac{a_s}{F_s} = \frac{-j\omega^2}{(K_s - M_s\omega^2) + jC_s\omega} \qquad (15)$$

where *(j)* is the imaginary unit. Figure 8 displays the results of the parameter estimation over a frequency range from 200 Hz to 550 Hz and 10 Hz to 200 Hz, enclosing the seal response motions around the dominant natural frequencies. The graphs also include the identified parameters in SI units. Table 3 presents the identified coefficients in English units. Clearly, for the frequency span of 10 Hz to 200 Hz, a linear mechanical system model does not best represent the test data.

Note that none of the identification processes renders the brush seal stiffness coefficient derived from static load measurements, although the lowest natural frequency (53 Hz) is larger than the predicted value of 36.5 Hz for the seal fixture alone. More importantly, the experimental results demonstrate that a linear spring and viscous damping model does not represent well the seal dynamic performance at low frequencies.

CONCLUSIONS

When compared to labyrinth seals, brush seals restrict more secondary flow leakage and allow larger rotor vibrations in less axial space. Presently, shoed brush seals are also able to handle reverse shaft rotations; and with the major advantages of reducing wear and eliminating hot thermal spots due to their non contacting operation.

The experiments demonstrate that, in range of applied loads from one to eight pounds, the seal static displacements are proportional to the applied load. Thus, seal flexibilities are readily obtained with accuracy. Static stiffness coefficients are understandably larger for the test procedure which did not perturb (no tapping) the seal while the loading process continued. In this case, the inherent stick-slip between the bristles apparently aids to stiffen the brush seal. The brush seal (average) direct stiffness *(K_s)* resulting from the tests with tapping and not tapping is 231.6 lb/in and 331.2 lb/in, respectively. The seal shows a cross-coupling structural stiffness *(k_s)* at approximately 15% of the direct stiffness coefficient for both test procedures. The simple beam model effectively predicts the stiffness of the brush seal disregarding the dry friction effects.

Impact tests evidence a non-linear behavior of the brush seal dynamic response due to the effects of the dry friction arising from bristle-to-bristle and bristles-to-back plate interaction. This characteristic makes a viscous damping model not suitable for brush seal damping response prediction at low frequencies (~50 Hz). A comprehensive analysis for prediction of the dynamic forced response of shoe-brush seal is also available [7]. A test rig, currently under construction, will allow multi-frequency tests under gas pressurized conditions. The aims are to validate computational predictions and offer reliable test data demonstrating the shoed brush seal operation.

ACKNOWLEDGEMENTS

Thanks to Advanced Turbomachinery Solutions for the financial support. The assistance of Mr. Heber Lemon, graduates student, in developing the simple brush seal stiffness model is also acknowledged.

REFERENCES

[1] Basu, P., Datta, A., Johnson, R., Loewenthal, R., Short, J., 1996, "Hysteresis and Stiffening Effects of Conventional Brush Seals," Journal of Propulsion and Power, **10**, pp. 569-575.

[2] Chupp, R., and Dowler C., 1993, "Performance Characteristics of Brush Seals for Limited-Life Engines," ASME Journal of Engineering for Gas Turbines and Power, **115**, pp. 390-396.

[3] Chupp, R., Raymond, E., and Nelson, P., "Evaluation of Brush Seals for Limited-Life Engines," Journal of Propulsion and Power, **9**, pp. 113-119.

[4] Fellenstein, J. A., Delacorte, C., 1996, "A New Tribological Test for Candidate Brush Seal Material Evaluation," Tribology Transactions, **39**, pp. 173-179

[5] Childs, D., and Vance, J. M., 1997, "Annular Gas and Rotordynamics of Compressors and Turbines," Proceedings of the 26th Turbomachinery Symposium, pp. 201-220.

[6] Justak, J., 2000, "*Hybrid Brush Seal Capable of Reverse Rotation*," Proposal to NAVY SBIR Program, Advance Turbomachinery Solutions, Fla.

[7] San Andrés, L., 2003, "Analysis of Performance and Rotordynamic Force Coefficients of Brush Seals with Reverse Rotation Ability," Final Report to Advanced Turbomachinery Solutions (ATS), March.

Table 1 Test shoed-brush seal geometry and parameters

Bristle diameter, d_b $(I=\pi d_b^4/64)$	0.0021 in
Bristle free length, L	0.3982 in
Bristle lay angle, θ	42.5 degrees
Pad length, L_p	0.972 in
Number of bristles per row, N_b	418
Number of rows, N_r	10
Number of pads, N_{pad}	36
Rotor inner diameter, D	11.14 in
Bristle modulus of elasticity, E	32.6 x 10^6 psi
Bristle position of first weld	100 (24% pad)
Bristle position of second weld	300 (71% pad)
Number of bristles per weld	8

Table2 Identified flexibility and stiffness coefficients for brush seal

Parameters Description	f_{sXX} (in/lb)	f_{sXY} (in/lb)	K_s (lb/in)	k_s (lb/in)	k_s/K_s (%)	Range* Force (lb)	Range* Deflection (in)
Tests with tapping	0.0044	-0.0006	231.6	31.6	14	0.984 to 8.031	0.0014 to 0.0316
r^2 (correlation coefficient)	0.992	0.884					
Average Uncertainty	0.0003	0.0002	18.5	9.8		0.001	5.10^{-5}
Tests non tapping	0.0031	-0.0005	331.2	53.4	16	2.036 to 9.035	0.0009 to 0.0271
r^2 (correlation coefficient)	0.984	0.859					
Average Uncertainty	0.0005	0.0003	57.0	33.0		0.001	5.10^{-5}

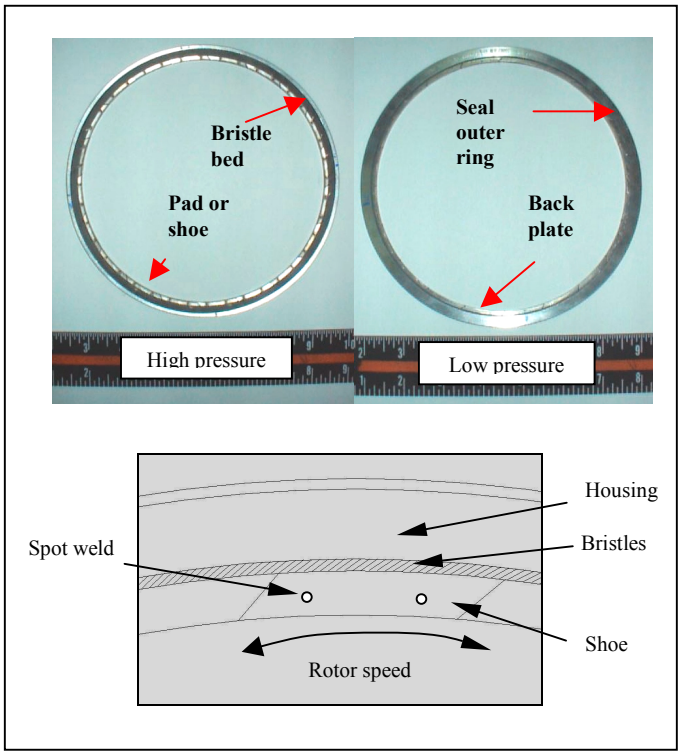

Figure 1 Shoed-brush seal with reverse rotation ability

Table 3 Identified force coefficients for brush seal from multiple impact tests. Frequency range 200 Hz to 550 Hz & 10 Hz to 200 Hz

		200-500 (Hz)	10-200 (Hz)
Stiffness, K_s	[lbf/in]	14,510	863
Damping, C_s	[lbf.s/in]	0.71	1.45
Mass, M_s	[lb]	0.85	3.05
Peak frequency, f_n	[Hz]	408	53
Damping ratio, ζ		0.063	0.28
correlation coefficient	r^2	0.98	0.67

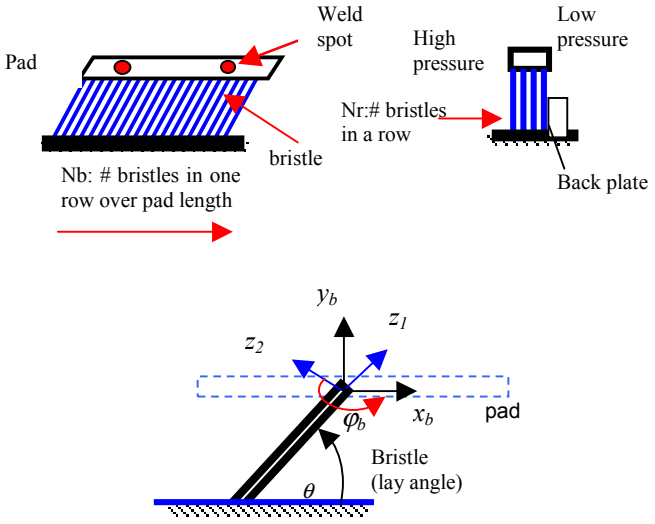

Figure 2 Nomenclature for shoed-brush seal stiffness prediction

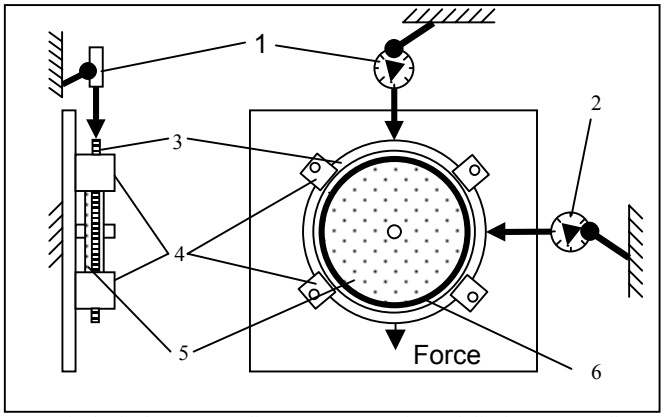

1.Vertical Displacement Indicator 2.Horizontal displacement Indicator
1. Guide posts 2. Metal Ring Support
3. Test Disk 4. Brush Seal

Figure 3 Schematic view of test fixture for shoed brush seal

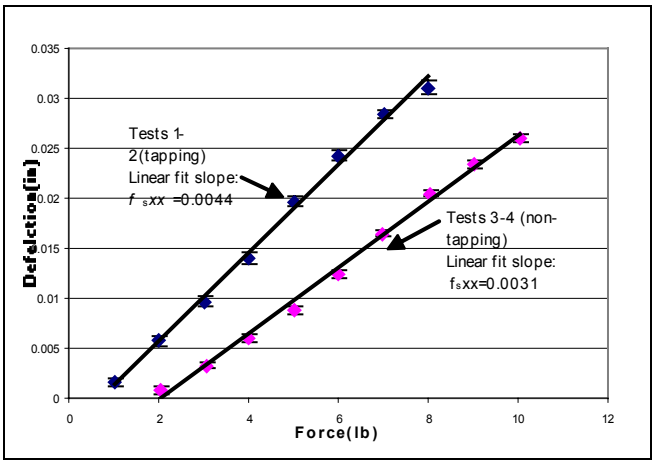

Figure 4 Seal principal deflections versus applied load (Tests 1-2: tapping, 3-4: non-tapping).

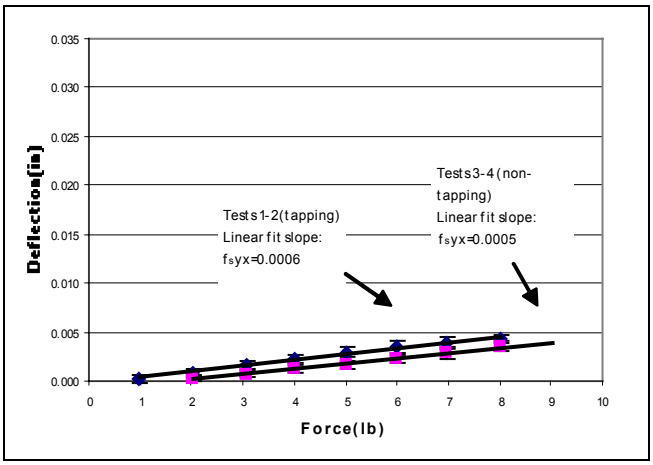

Figure 5 Seal cross-deflections versus applied load (tapping, non-tapping)

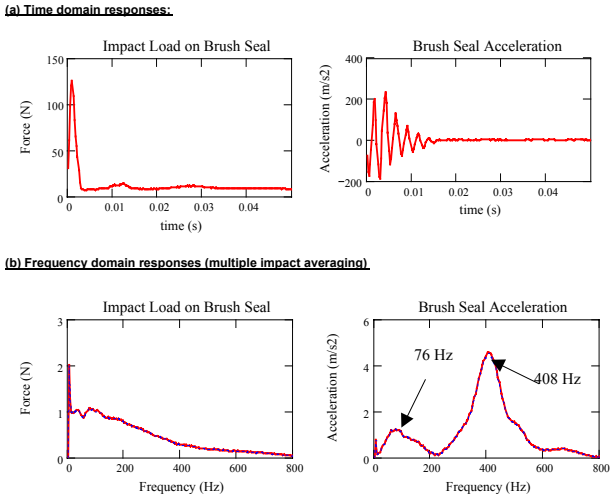

Figure 6 Impact response of brush seal (a) load and seal displacement versus time; (b) 20-impact average FFT of load and displacement

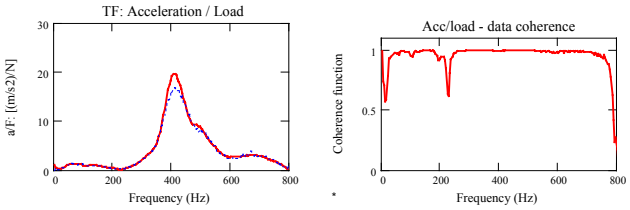

Figure 7 Transfer function (acceleration/load) and coherence function from 20 impact response experiments

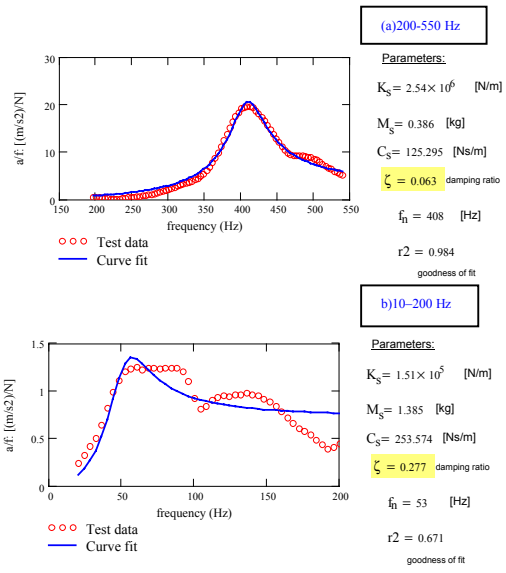

Figure 8 Model and experimental transfer function (acceleration/load) for a frequency range (a) from 200 Hz to 550 Hz and (b) from 10 Hz to 200 Hz